Ultrasound in Med. & Biol., Vol. 00, No. 00, pp. 1–14, 2020

0301-5629/$ - see front matter

https://doi.org/10.1016/j.ultrasmedbio.2019.10.023

● *Original Contribution*

TEMPERATURE DEPENDENCE OF TISSUE THERMAL PARAMETERS SHOULD BE CONSIDERED IN THE THERMAL LESION PREDICTION IN HIGH-INTENSITY FOCUSED ULTRASOUND SURGERY

SITARAMANJANEYA REDDY GUNTUR,* and MIN JOO CHOI†

* Department of Biomedical Engineering, Vignan's Foundation for Science, Technology and Research, Vadlamudi, Guntur, India; and † Department of Medicine, School of Medicine, Jeju National University, Jeju, Republic of Korea

(*Received* 2 *June* 2019; *revised* 21 *October* 2019; *in final from* 26 *October* 2019)

Abstract—This study considers the temperature-dependent thermal parameters (specific heat capacity, thermal diffusivity and thermal conductivity) used when predicting the temperature rise of tissue exposed to high-intensity focused ultrasound (HIFU). Numerical analysis was performed using the Khokhlov–Zabolotskaya–Kuznetsov equation coupled with a bioheat transfer function. The thermal parameters were set as the functions of temperature using experimental data. The results revealed that, for liver tissue exposed to HIFU with a focal intensity of 3000 W/cm^2 for 10 s, the predicted focal temperature rise was 23% lower and the thermal lesion area 41% smaller than those predicted without considering the temperature dependence. The prediction was validated by experimental observations on thermal lesions visualized in a tissue-mimicking phantom. The present results suggest that temperature-dependent thermal parameters should be considered in the prediction of HIFU-induced temperature rise to avoid lowering ultrasonic output settings for HIFU surgery. The aim of the present study was to investigate how significantly the temperature dependence of the thermal parameters affects the thermal dose imposed on the tissue by a typical clinical HIFU device. A numerical simulation was performed using a thermo-acoustic algorithm coupling the non-linear Khokhlov–Zabolotskaya–Kuznetsov (KZK) equation (Meaney et al. 1998; Filonenko and Khokhlova 2001) and a bioheat transfer (BHT) equation (Pennes 1948). Thermal parameters of liver tissue were modeled in the present study as functions of temperature and were incorporated into the BHT equation to compensate for the variations in thermal parameters with temperature. Experimental validation was achieved by comparing the predictions with the thermal lesions formed in the tissue-mimicking phantoms. (E-mail: mjchoi@jejunu.ac.kr)

Key Words: **High-intensity focused ultrasound, Thermal parameter, Temperature dependence, Temperature prediction, Thermal lesion.**

INTRODUCTION

High-intensity focused ultrasound (HIFU) surgery is a promising non-invasive method used to thermally ablate solid tumors lying deep under the skin surface (Hill and ter Haar 1995). HIFU is used in the clinical treatment of prostate, liver and breast tumors and uterine fibroids (ter Harr et al. 1989; Vaezy et al. 1999; Zhou 2011). The primary mechanism underlying HIFU surgery is based on ultrasonic thermal effects. Technical difficulties in accurate non-invasive temperature monitoring prevent clinical users from optimizing thermal dose and limit the popularization of clinical applications of HIFU surgery.

Address correspondence to: Min Joo Choi, Department of Medicine, School of Medicine, Jeju National University, 102 Jejudahakro, Jeju 63243, Republic of Korea. E-mail: mjchoi@jejunu.ac.kr

It looks promising that magnetic resonance (MR) thermometry will overcome the problems and enable us to monitor or map local temperature changes during thermal therapy (Funaki et al. 2009; Kobus and McDannold 2015). The technology has recently been employed in clinical devices to optimize HIFU exposure; for example, the Exablate Neuro (InSightec Ltd., Tirat Carmel, Israel) is used to treat target tissues located deep within the brain of patients with Parkinson's disease (Gallay et al. 2016). However, it is too expensive and has technical shortcomings. MR thermometry does not provide absolute temperatures but offers relative differences from initial states. Current image quality is limited to a spatial resolution of about 0.5 mm^3 and a temperature resolution of ±1°C (Rieke and Pauly 2008; Fite et al. 2012). It is not fast enough to perform real-time thermal

imaging, which may give rise to significant artifacts in moving organs (DeSenneville et al. 2007).

In these circumstances, numerical simulation plays a practically useful role in treatment planning and provides clinical users with critical information for improving the clinical efficacy of HIFU surgery. The HIFU-induced temperature distribution in the target tissue can be reasonably predicted by coupling the radiated acoustic field with a heat transfer function (Damianou and Hynynen 1994). The thermal lesion can be estimated from the temperature distribution according to clinical thermal dose criteria (Sapareto and Dewey 1984).

Few studies have addressed the influence of temperature-dependent tissue parameters on thermal effects during thermotherapy (Kolios et al. 1999; Dragonu et al. 2009). However, existing methods for the prediction of temperature distribution in tissue exposed to HIFU take tissue thermal parameters (such as, specific heat capacity, thermal diffusivity and thermal conductivity) as constants, often measured at room temperature. Experimental observation revealed that these tissue properties vary significantly with temperature (Guntur et al. 2013). There are other factors that depend on temperature, including acoustic parameters (speed of sound, absorption, non-linear parameter (B/A), *etc.*) and perfusion associated with the thermal effect of HIFU on tissues. As reported in previous studies for liver tissues, the attenuation coefficient and B/A increase with temperature (Choi et al. 2011). The blood perfusion rate near tissue heated to coagulating temperatures up to 90°C was observed to increase as high as 20 times the normal perfusion rate (Zhang et al. 2011).

As outlined in Table 1, for the temperature range 25−90°C, the thermal parameters relative to those at room temperature varied from 0.949−1.143 for specific heat capacity, from 0.904−1.320 for thermal conductivity and from 0.959−1.306 for thermal diffusivity. Our pilot study indicated that the temperature-dependent thermal parameters significantly influenced the focal temperature rise when tissues were exposed to the acoustic field used for HIFU surgery (Guntur and Choi 2015). Yet few studies have considered the influence of the temperature-dependent parameters, particularly the thermal parameters, when predicting tissue temperature distributions and the resulting thermal lesion formed in the target tissue.

METHODS

The KZK equation was employed to calculate nonlinear acoustic propagation in tissues exposed to HIFU (Meaney et al. 1998; Filonenko and Khokhlova 2001). The resulting temperature distribution formed in the tissues was estimated by coupling the calculated acoustic intensity with the BHT function (Pennes 1948) as an external heat source. Tissue thermal parameters were incorporated as functions of temperature into the BHT function to compensate for the temperature dependence of the thermal parameters.

The present study considers a clinical HIFU field that is produced by a focused transducer (Sonic Concepts, Woodinville, Inc., WA, USA) and resonates at 1.1 MHz with an aperture diameter of 64 mm and a focal depth of 62.26 mm. The transducer is driven to deliver HIFU to *ex vivo* liver tissue. The numerical calculation for the focusing acoustic field was conducted on the 2-D ($r-z$) axisymmetric propagation geometry, as illustrated in Figure 1. The details for the numerical simulation are described in our previous articles (Guntur 2013; Guntur and Choi 2015).

The temperature distribution developed in the liver tissue exposed to HIFU was predicted by the BHT (Pennes 1948) as

$$\rho \cdot C \cdot \frac{\partial T}{\partial t} = \kappa \cdot \nabla^2 T + H - C_b \cdot W \cdot T \qquad (1)$$

where ρ and C are the density (kg/m^3) and the specific heat capacity (J/kg/K) of tissue, respectively, κ is the thermal conductivity of the tissue (W/m/K), T is the temperature of tissue (°C), t is the time, W is the perfusion rate in the heated region of the tissue (kg/s/m^3), C_b is the specific heat capacity (J/kg/K) of blood, and H is the heat production rate (W/m^3), which is approximated as

$$H = 2 \cdot \alpha \cdot I \qquad (2)$$

where α is the attenuation coefficient (Np/m) of tissue, and I is the acoustic intensity (W/m^2) calculated using the KZK equation. Equation (2) states that the BHT function (1) is effectively coupled with the acoustic field via the acoustic intensity I transformed into the heat production rate H. As described in the Introduction, the

Table 1. Thermal parameters of *ex vivo* live tissue measured at temperatures ranging from 25−90°C (Guntur et al. 2013)

Parameter	25°C	30°C	35°C	40°C	45°C	50°C	55°C	60°C	65°C	70°C	75°C	80°C	85°C	90°C
Specific heat capacity (mJ/m^3·K)	3.654	3.597	3.567	3.576	3.601	3.660	3.710	3.773	3.849	3.922	4.010	4.104	4.177	4.296
Relative to 25°C	-	0.985	0.976	0.979	0.985	1.002	1.015	1.033	1.053	1.073	1.097	1.123	1.143	1.176
Thermal conductivity (W/(m·K))	0.546	0.528	0.520	0.525	0.529	0.538	0.559	0.570	0.585	0.610	0.633	0.665	0.702	0.759
Relative to 25°C	-	0.967	0.952	0.962	0.969	0.985	1.024	1.044	1.072	1.117	1.159	1.22	1.285	1.390
Thermal diffusivity (mm^2/s)	0.144	0.142	0.141	0.141	0.142	0.143	0.145	0.148	0.152	0.158	0.164	0.171	0.181	0.192
Relative to 25°C	-	0.986	0.979	0.979	0.986	0.993	1.007	1.027	1.056	1.097	1.139	1.1875	1.257	1.333

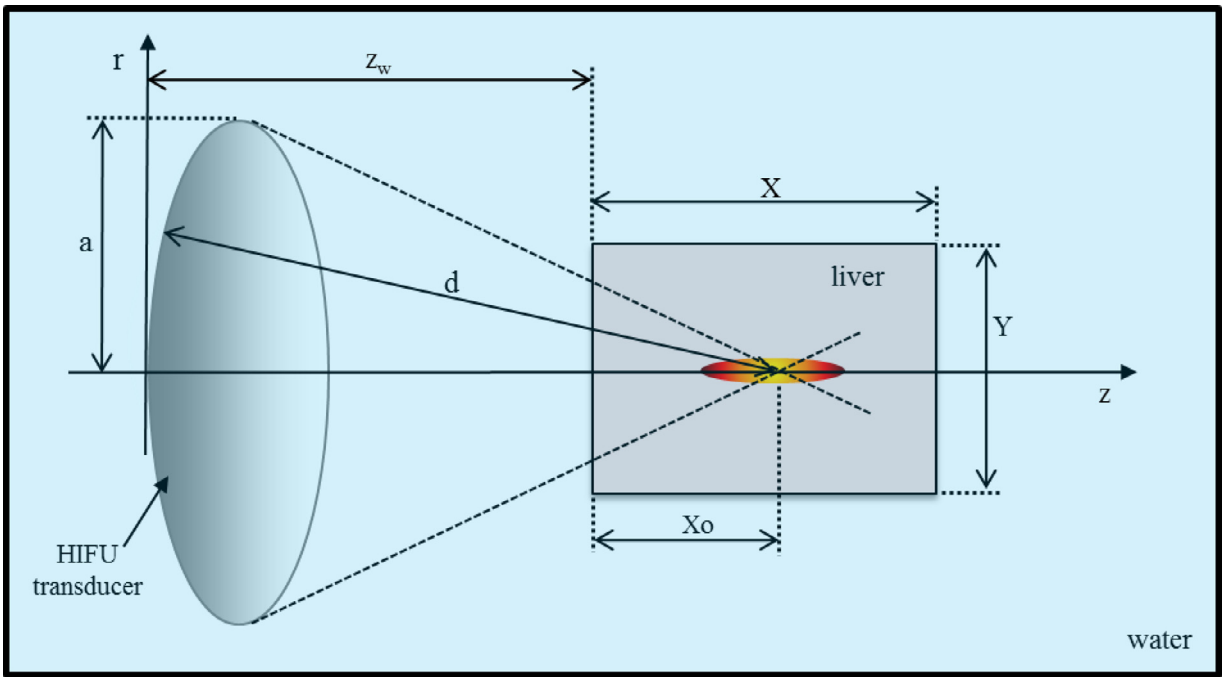

Fig. 1. Geometric configuration for the numerical simulation of the 2-D ($r-z$ plane) axisymmetric high-intensity focused ultrasound (HIFU) field to which liver tissue was exposed. All boundary surfaces serve as perfectly absorbing boundary conditions: a = transducer aperture radius (32 mm), d = geometrical focal length (62.26 mm), X = depth of the liver tissue (40 mm), Y = width of the liver tissue (40 mm), X_o = depth to the focus in the liver tissue (20 mm) and z_w = material transition distance (42.26 mm).

tissue thermal parameters (C and κ) are conventionally taken to be constants when numerically solving eqn (1). In the present study, the prediction considered the thermal parameters varying with temperature (Table 1), incorporating them into eqn (1) as functions of temperature. As described in Guntur et al. (2013), the measured thermal parameters characteristically exhibit the same pattern with temperature, drawing asymmetrical quasi-parabolic curves with their convex downward (see Fig. 3 of Guntur et al. 2013). By combination of two index functions (called "quasi-parabolic") on either side of the turning temperature ($T = T_o$), the characteristic curve, $Y(T)$, can be mathematically expressed as

$$Y(T) = A_{1O}\,(T - T_O)^{m_1} + B \quad \text{for} \quad T_1 \le T \le T_O \tag{3}$$

$$Y(T) = A_{O2}\,(T - T_O)^{m_2} + B \quad \text{for} \quad T_O \le T \le T_2 \tag{4}$$

where T is temperature, T_1 and T_2 are respectively the lowest and highest temperatures considered, T_o is the turning temperature, and $B = Y(T_o)$, A_{1O} and m_1 are determined from the best fit to the data measured for $T_1 \le T \le T_o$, and, in the same way, A_{O2} and m_2 are determined from the best fit to the data for $T_o \le T \le T_2$. Note that A_{1O}, A_{O2}, m_1 and m_2 are all positive for modeling the quasi-parabolic curves. A least-mean-squares method can be used to estimate A_{1O}, A_{O2}, m_1 and m_2; the details are given in the Appendix. Table 2 lists the values of B, T_o, A_{1O}, A_{O2}, m_1 and m_2, which were best fitted to the data in Table 1 measured for *ex vivo* liver tissue (Guntur et al. 2013).

Figure 2 is a flow diagram designed for compensating the temperature dependent tissue thermal parameters when predicting the temperature distribution induced in tissue by HIFU. Note that the square brackets [] denote the matrix forms of the parameters (T, I, H, C and κ). The parameters represent the values at each grid of the entire calculation region and therefore have the same dimensions. For instance, [T] represents the array of

Table 2. Values of the parameters (B, T_o, A_{1O}, A_{O2}, m_1 and m_2) that render the empirical quasi-parabolic functions (eqns [3] and [4]) best-fitted to the thermal parameters with temperature measured for *ex vivo* liver tissue (Guntur et al. 2013)

Thermal parameter	B	T_o (°C)	A_{1O}	A_{O2}	m_1	m_2
Specific heat capacity (mJ/m^3/K)	3.567	35	0.11×10^{-2}	0.541×10^{-3}	1.698	1.823
Thermal conductivity (W/m/K)	0.520	35	0.341×10^{-3}	0.270×10^{-3}	1.725	1.642
Thermal diffusivity (mm^2/s)	0.141	35	0.725×10^{-4}	0.806×10^{-5}	1.615	2.151

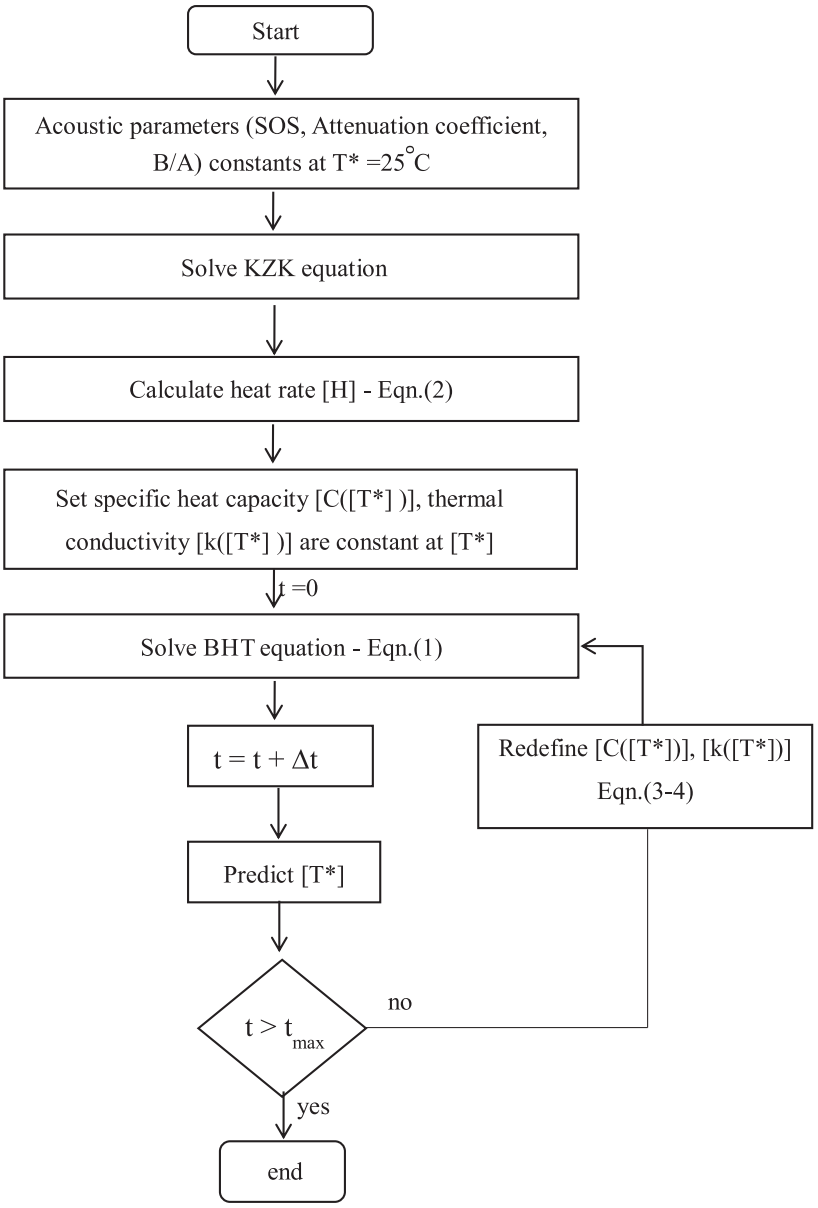

Fig. 2. Flow diagram of the simulation model for compensating temperature-dependent thermal properties. [*T**] is tissue temperature (initially 25°C). The temperatures considered in this study ranged from ambient temperature (25°C) to 90°C. Temporal step size $\Delta t = 0.01$ s. Note that the square brackets [] denote a matrix whose element represents the value at each grid of the entire calculation region. BHT = bio-heat transfer; KZK Khokhlov–Zabolotskaya–Kuznetsov; SOS = speed of sound.

tissue temperatures predicted at the grids of the entire region (r_i, z_j) for calculation (see Fig. 1). The elements of [T] were assumed initially to be the constant value, that is, the room temperature of 25°C ([T_i] = 25°C). The first stage of numerical calculation solves the KZK non-linear equation to calculate the intensity field [I] = I (r_i, z_j), from which the rate of heat production [H] = H (r_i, z_j) can be obtained using eqn (2). Note that the values of the parameters and coefficients used in the KZK equation were those measured or defined at room temperature (25°C). Once [H] is calculated, the BHT function is solved in the second stage for the HIFU exposure time of t_{max}. The detailed description for solving the BHT function is given in our previous articles (Guntur 2013; Guntur and Choi 2015). In the first step ($t = 0$), the matrix form of the tissue thermal parameters [C] for heat capacity and [k] for heat conductivity are set to constants measured at room temperature (25°C) over the entire region of calculation. When the first step is completed and the temperature field [T] at $t = \Delta t$ is predicted, the thermal

Table 3. Values of the acoustic parameters of water and liver used for numerical prediction of the HIFU field used to irradiate *ex vivo* liver tissue at 25°C, together with those of TM PAG

Parameters	Symbol	Water	Tissue	TM PAG*	Unit
Small-signal sound speed	c	1,482	1,575	1,579	m/s
Density	ρ	1,000	1,060	1,057	kg/m^3
Absorption (at 1 MHz)	α	0.0022	0.52	0.51	dB/cm
Exponent of absorption versus frequency	ή	1	1	1	-
Non-linear parameter	β	4.9	6.8	6.2	-

HIFU = high-intensity focused ultrasound; TM PAG = tissue-mimicking polyacrylamide gel.

* Values from Guntur and Choi (2014).

parameters [C] and [k] are updated according to eqns (3) and (4) for the predicted temperature field of [T]. The [C] and [κ], from the second step ($t = 2\Delta t$) of solving the BHT function are no longer constants over the entire region but spatially different depending on the predicted [T]. This process is repeated while t is less than t_{max}.

Numerical simulation was carried out for an *ex vivo* liver tissue exposed to a continuous (duty factor = 100%) HIFU field with a focal peak pressure of 17.5 MPa (or a focal intensity of 3000 W/cm^2). The transducer was driven continuously for 10 s to deliver the HIFU to the liver tissue. The values of the acoustic parameters of water and the liver tissue used in the KZK equation are listed in Table 3.The liver was assumed to be homogenous. The number of harmonics was 128 for prediction of the non-linear acoustic field. The entire computational region is the inner square of ($0 \le z \le 2d$, $-a \le r \le a$), as illustrated in Figure 1, and the spatial step sizes were $dr = 0.022$ mm and $dz = 0.012$ mm. The step sizes (0.012−0.022 mm) represent the wavelengths of 125−68 MHz, and so aliasing may appear in the numerical simulation that considers 128 harmonics of up to 128 MHz. The selection of the step sizes was justified by the contribution of very high harmonics (>68 MHz) observed to be almost negligible. The heat production rate [H] was calculated in the first stage and was taken to the second stage to solve the BHT function. The BHT differential equation was solved by a second-order finite difference discretization with Dirichlet boundary conditions. The temperature prediction included an additional 5 s to include natural cooling time after the HIFU irradiation was off. The temporal step size dt was set to 0.01 s. The perfusion was neglected, namely, $W = 0$ in eqn (1), which is reasonable as the prediction was performed for an *ex vivo* liver.

To validate the prediction, the HIFU-induced thermal lesions were visualized in a tissue-mimicking polyacrylamide gel (TM PAG) (Guntur and Choi 2014) and then were compared with predictions. The measured values of the temperature-dependent thermal parameters of TM PAG for the temperature range 25−90°C are listed in Table 4 and, as observed, are close to those of the liver tissue (Table 1). The experimental arrangement for visualizing the thermal lesions formed in the TM PAG exposed to the HIFU field was described by Park et al. (2010) and Choi et al. (2013). The polyacrylamide gel (PAG) sample housed in a rectangular hexahedral acrylic chamber ($40 \times 40 \times 40$ mm^3) was immersed in a water tank and positioned so that its center coincided with the focus of HIFU transducer (Sonic Concepts, Inc., Woodinville, WA, USA) under the guidance of two Charged Coupled Device (CCD) cameras. To produce thermal lesions in the PAG, the HIFU production system was set to operate in continuous wave mode, with a focal peak pressure of 17.5 MPa (focal intensity = 3000 W/cm^2) exposure for 1, 2, 3, 5 and 10 s. The focal pressure was measured in water using an optical fiber hydrophone (FOPH-2000, RP Acoustics, Leutenbach, Germany), and the focal intensity (spatial peak temporal average intensity, I_{spta}) was calculated via the pulse intensity integral of the measured focal pressure waveform (International Electrotechnical Commission Norm 1102). HIFU exposure was controlled on a computer with software programmed under the LabVIEW environment (NI PXI-1042, National Instruments, Austin, TX, USA). The optical images of the thermal lesion visualized in the PAG sample were recorded with a CCD camera.

RESULTS

Figure 3 illustrates the steady-state acoustic pressure distribution $p(z, r)$ predicted in the liver tissue exposed to the HIFU field, produced by the focal peak pressure of 17.5 MPa (focal intensity = 3000 W/cm^2).

Table 4. Thermal parameters of TM PAG measured at temperatures ranging from 25−90°C

Parameter	25°C	30°C	35°C	40°C	45°C	50°C	55°C	60°C	65°C	70°C	75°C	80°C	85°C	90°C
Specific heat capacity ($mJ/m^3.K$)	3.933	3.861	3.817	3.807	3.803	3.823	3.852	3.862	3.900	3.950	4.019	4.073	4.151	4.272
Relative to 25°C	-	0.982	0.971	0.968	0.967	0.972	0.979	0.982	0.992	1.004	1.022	1.036	1.055	1.086
Thermal conductivity (W/(m.K))	0.562	0.554	0.549	0.547	0.551	0.560	0.568	0.581	0.593	0.611	0.637	0.657	0.698	1.753
Relative to 25°C	-	0.986	0.977	0.973	0.980	0.996	1.011	1.034	1.055	1.087	1.133	1.169	1.241	1.340
Thermal diffusivity (mm^2/s)	0.151	0.148	0.146	0.144	0.146	0.147	0.148	0.149	1.150	0.154	0.159	0.165	0.173	0.193
Relative to 25°C	-	0.980	0.967	0.954	0.967	0.974	0.980	0.987	0.993	1.020	1.053	1.093	1.146	1.278

TM PAG = tissue-mimicking polyacrylamide gel.

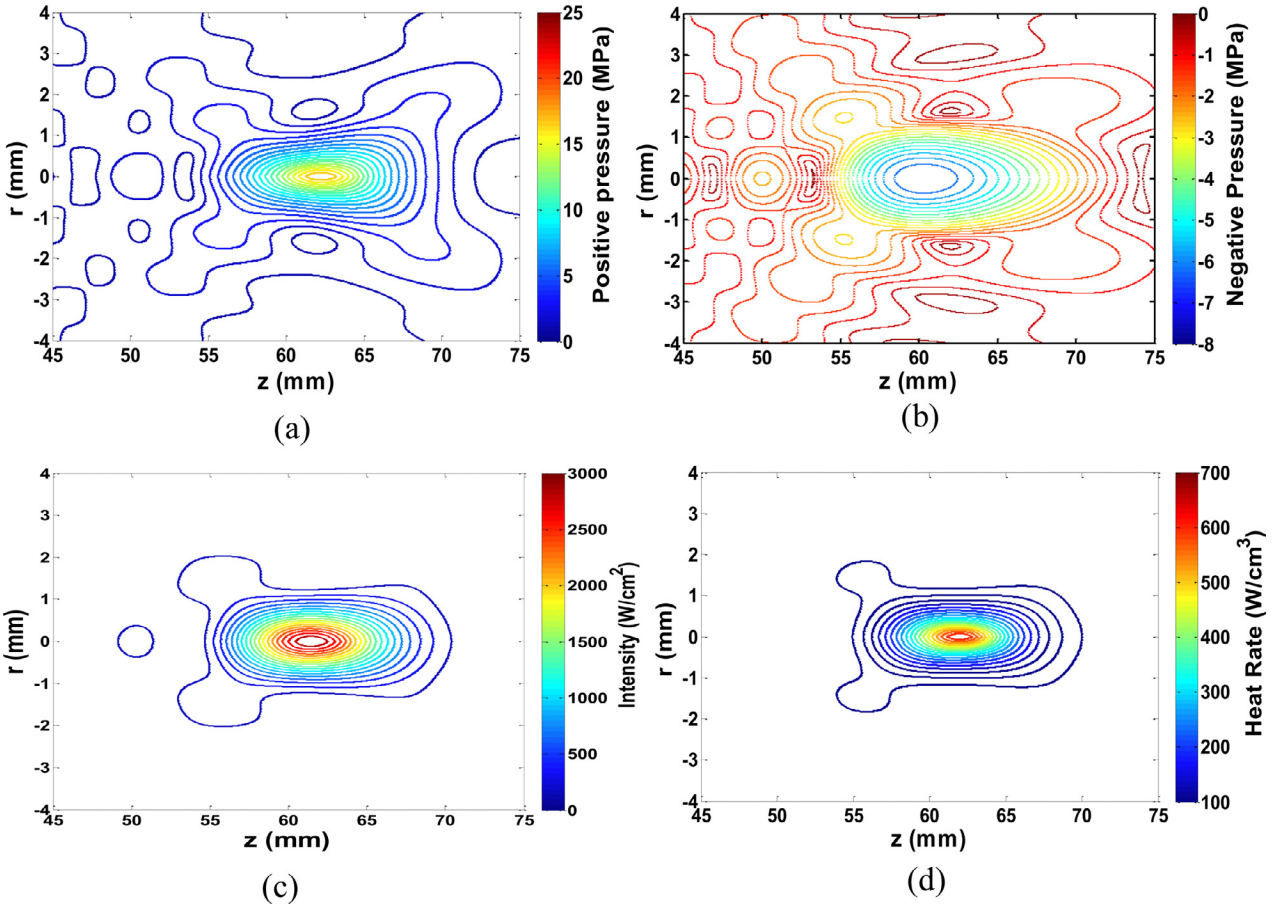

Fig. 3. Non-linear acoustic field and the heat production rate predicted throughout the focus (in liver exposed for 10 s to a continuous high-intensity focused ultrasound field with a focal pressure of 17.5 MPa. (a) Peak positive pressure $p^{+}(z, r)$. (b) Peak negative pressure $p^{-}(z, r)$. (c) Intensity $I(z, r)$. (d) Heat production rate $H(z, r)$

The peak positive pressure field $p^{+}(r, z)$ and the peak negative pressure field $p^{-}(r, z)$ are plotted in Figure 3a and b, respectively. The spatial distribution of the heat production rate $H(r, z)$ is plotted in Figure 3d, which was calculated using eqn (2) from the intensity field I(r, z) shown in Figure 3c.The maximum heat production rate at the focus was predicted to be 575 W/cm^3.

Figure 4 illustrates the temperature distribution $T(r, z)$ (contour in the left panel and image in the right) in the liver tissue exposed to the HIFU field (focal pressure = 17.5 MPa), predicted at 1, 2, 3, 5, 7, 10 and 15 s. The 15-s point represents the moment of 5 s of natural cooling after termination of ultrasonic irradiation. Figure 4a is the $T(r, z)$ calculated using the conventional method, which is eqn (1), with the constant tissue thermal parameters (specific heat capacity and thermal conductivity) measured at room temperature (25°C), while Figure 4b illustrates the $T(r, z)$ predicted with the thermal parameters as functions of temperature.The area within which the temperature was higher than the threshold temperature of 60°C may be regarded as a possible thermal lesion. Figure 4 illustrates that the predicted potential thermal lesions have axially elongated ellipsoid shapes. The temporal variations of the temperature distributions in the vicinity of the focus are characteristically similar for the two methods. However, the thermal lesions are larger in the conventional method than the present compensation approach. The peak temperatures, located near the center of the lesion and coinciding with the HIFU beam focus, are also larger in the conventional prediction than the compensation method.

Figure 5 plots peak temperature at the focus along time in the liver tissue, clearly differentiating the present method from the conventional prediction. The focal temperature gradually increases in a logarithmic pattern with exposure time and reaches its maximum value of 90°C at 10 s in the conventional method, whereas it increases relatively less rapidly with time and reaches a maximum of not more than 71°C in the present model. This result indicates that the conventional method significantly overestimates the focal temperature (by >23%), compared with the present approach, which considers the temperature dependence of the tissue thermal parameters.

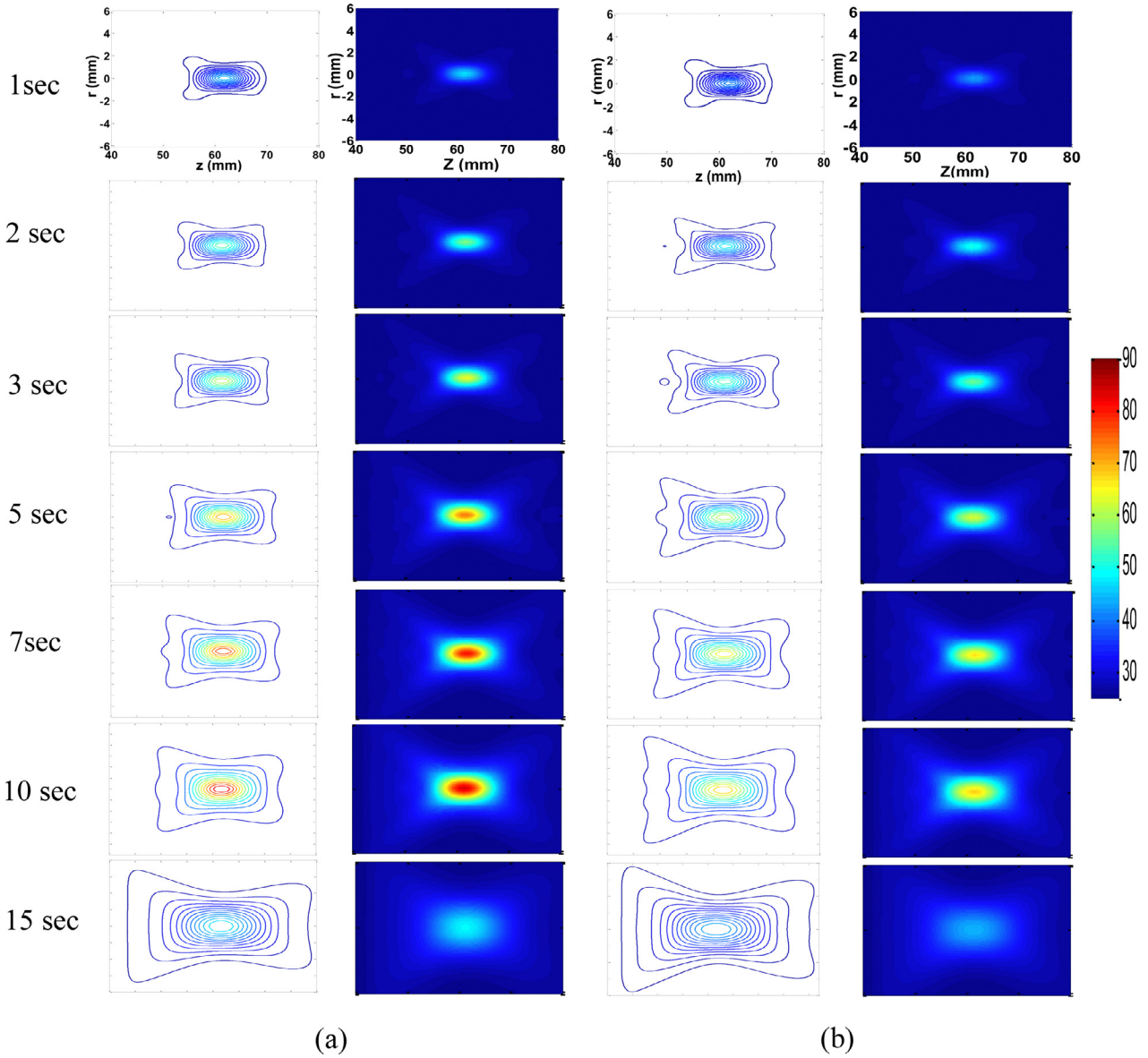

Fig. 4. Temperature contours (left) and images (right) of $T(z, r)$ in liver exposed to 1.1-MHz high-intensity focused ultrasound with a focal pressure of 17.5 MPa and followed by natural cooling. (a) By the conventional method with constant thermal parameters measured at room temperature (25˚C). (b) By the present model compensating for the temperature dependence of the thermal parameters, predicted at 1, 2, 3, 5, 7, 10 and 15 s.

To validate the present prediction, the predicted thermal lesions were compared to those experimentally observed in the TM PAG containing a thermosensitive protein (bovine serum albumin [BSA]) exposed to the same HIFU with a focal intensity of 3000 W/cm^2 for 10 s. The details of the TM PAG are found in Guntur and Choi (2014). Figure 6 illustrates the typical thermal lesions formed in the TM PAG observed after 1, 2, 3, 5, 7 and 10 s of exposure to HIFU, together with the image (at 15 s) after 5 s for natural cooling. The *white opaque area* represents the thermal lesion where the temperature is above the threshold (~60˚C) for protein denaturation. Note that the HIFU transducer (not shown) was located on the left-hand side of the images, as in the simulations (Figs. 3 and 4).

Figure 7a contrasts the thermal lesion boundaries for the conventional model (*short dots*), present model (*short dash dots*) and the experimental observation (*solid line*), which were drawn from the thermal lesions predicted (Fig. 4) and formed in the TM PAG (Fig. 6).The boundary of the thermal lesion was determined by the threshold temperature 60˚C, as noted in Figure 6. As illustrated in Figure 7a, the present prediction results in thermal lesions close to those of the experimental

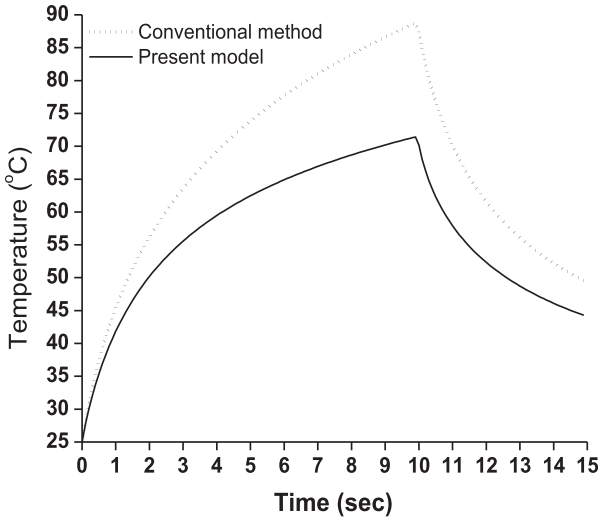

Fig. 5. Time history of the temperature at the focus in the liver exposed to the 1.1-MHz high-intensity focused ultrasound with a focal pressure of 17.5 MPa for 10 s, predicted by the present model (*solid line*) compensating for the temperature dependence of tissue thermal parameters and by the conventional method (*dotted line*) with constant thermal parameters defined at room temperature (25˚C).

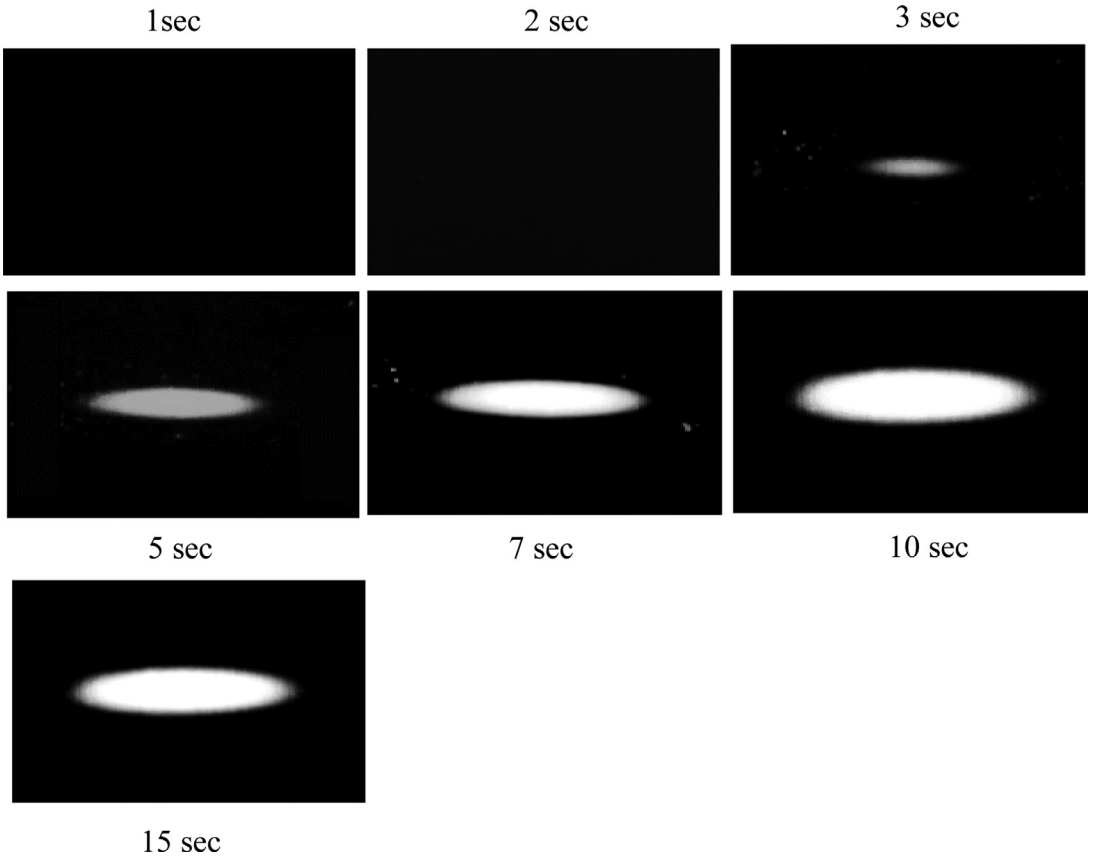

Fig. 6. Thermal lesions visualized in the bovine serum albumin (BSA) tissue-mimicking phantom (Guntur and Choi 2014) in which *white* represents the area of temperature above the threshold (~60 ˚C) for the protein BSA denaturation. The phantom was exposed to high-intensity focused ultrasound with a focal intensity of 3000 W/cm^2 for 10 s and was left for natural cooling.

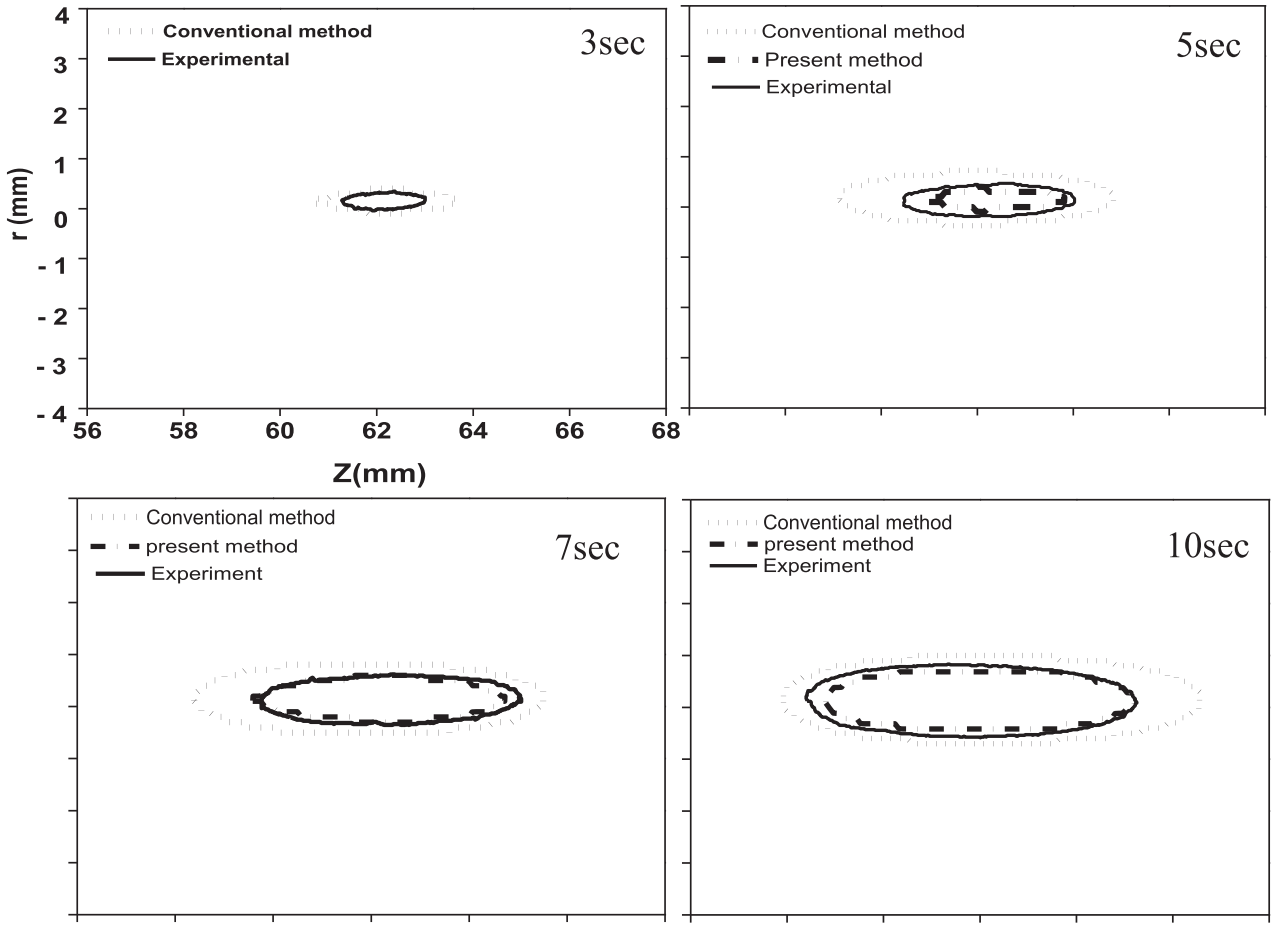

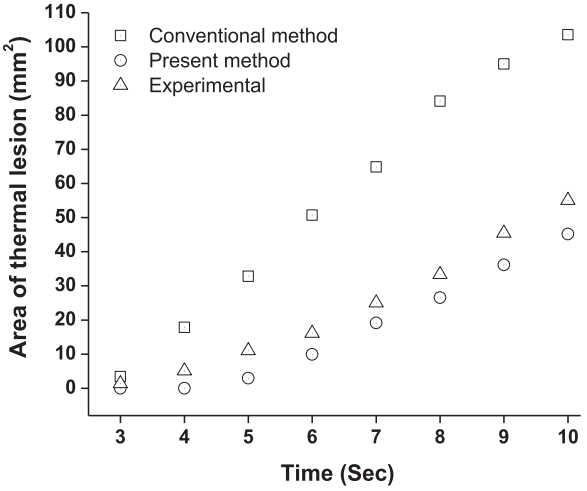

(b)

Fig. 7. Comparison of predictions (Fig. 4) and experimental observation (Fig. 6) of thermal lesions formed in liver exposed to a 1.1-MHz high-intensity focused ultrasound field with a focal pressure 17.5 MPa for 3, 5, 7 and 10 s. (a) Boundaries of the thermal lesions (note that the predictions were drawn for the images in Fig. 4 with a threshold temperature of 60˚C). (b) Calculated areas of the thermal lesions.

observation, while the conventional method exaggerates them. For quantitative comparison, the calculated areas of the thermal lesions were plotted against exposure time (Fig. 7b). As expected, lesion size increased with exposure time. The rate of increase is much larger in the conventional method than in the present model, while it is similar for the present model and the experimental observation. Compared with the experimental observation, the conventional method largely overestimated the lesion area, whereas the present model slightly underestimated the area. For instance, the lesion area at the exposure time of 10 s was predicted to be 4% smaller by the present model but 28 % larger by the conventional method, compared with what was observed in the phantom.

A popular way for identifying the thermal lesion often employs the thermal dose of 240 min at 43˚C (TD_{43} = 240 min), known to be a threshold level for tissue thermal necrosis (Bailey et al. 2003). Figure 8 illustrates the TD_{43} contour calculated for the temporal history of the T(r, z) shown in Fig. 4. The gray areas correspond to the region heated for more than 240 min at 43˚C is regarded to be thermal lesions.

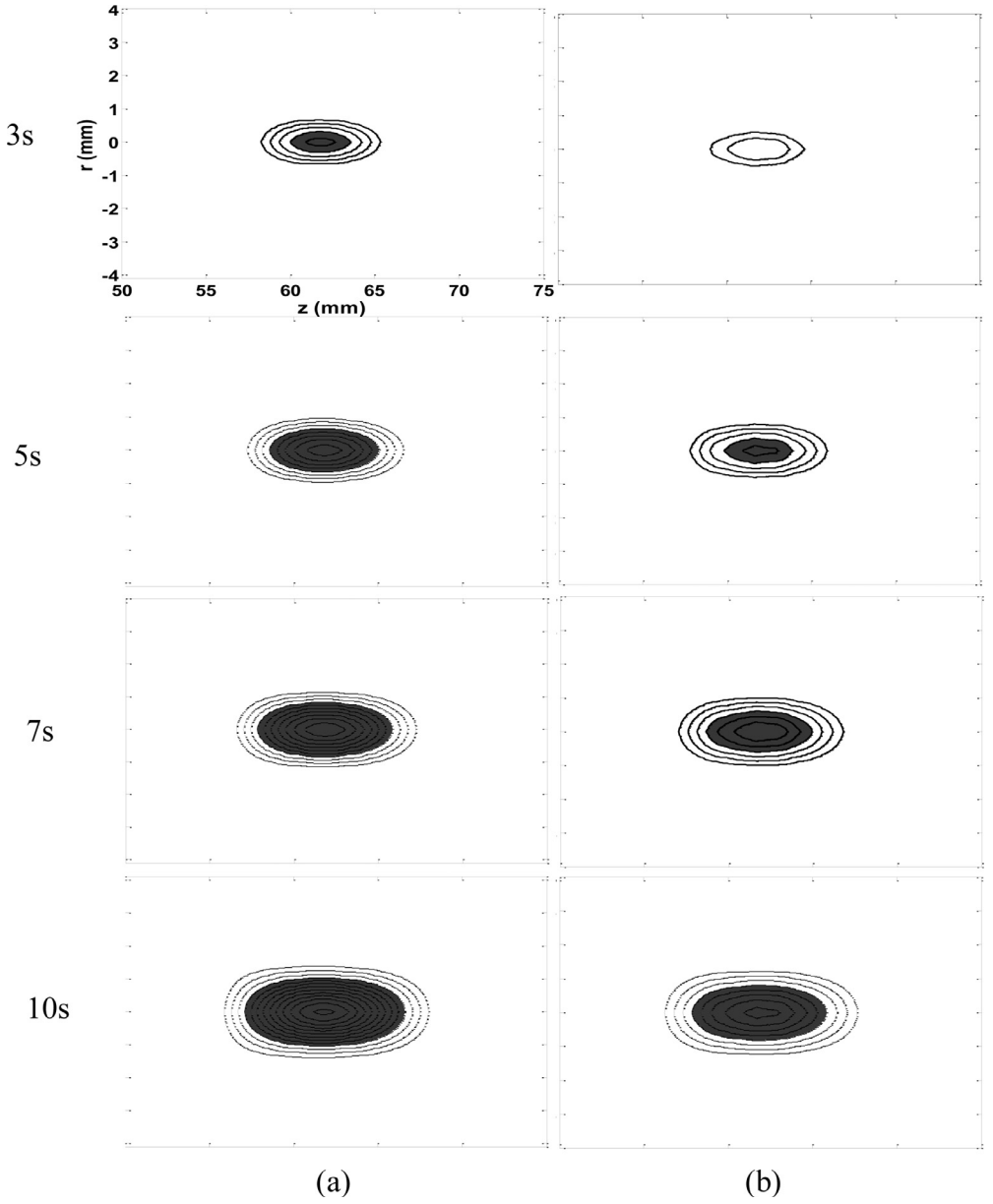

Fig. 8. Thermal dose TD_{43} contours formed in liver exposed for 10 s to a 1.1-MHz high-intensity focused ultrasound field with a focal pressure of 17.5 MPa. (a) Predicted by the conventional method with constant thermal parameters at room temperature (25˚C). (b) Predicted by the present model compensating for the temperature dependence of the thermal parameters. Note that the area colored *gray* (TD_{43} >240 min) represents tissue necrosis.

DISCUSSION

In conventional prediction of temperature distributions in tissues exposed to a clinical HIFU field, the tissue thermal parameters are taken as constants in solving the BHT equation (Meaney et al. 1998; Kolios et al. 1999; Lee and Yoon 2005; Heydari and Jahed 2009). Thermal parameters are considered to remain unchanged with temperature, and their values measured at room temperature are employed in conventional predictions. In contrast, the present approach allows thermal parameters to vary with temperature, as described in Guntur et al. (2013). The temperature elevations in tissue exposed to a typical clinical HIFU field predicted by the present method were found to be lower than those of the conventional method. Compared with the thermal lesions observed in the BSA tissue-mimicking phantom exposed to the same HIFU field, the present model predicts lesions similar to (slightly smaller than) the observations, whereas the conventional method predicts them significantly larger than the observations.

The overestimation of the conventional method is attributed to ignorance of the temperature dependence of the tissue thermal parameters. As formulated in eqn (1), the temporal gradient of temperature ($\partial T/\partial t$) is inversely proportional to the specific heat capacity (C) in the first term (κ/C)($\nabla^2 T/\rho$) and the second term ($1/C$)(H/ρ) on the right-hand side of eqn (1). As the tissue is heated to temperatures higher than 50˚C, C becomes larger than its nominal value measured at room temperature (3.654 mJ/m^3·K at 25˚C) (Table 1), and thus, $\partial T/\partial t$ decreases when compensating for the temperature dependence of C. As seen in the first term on the right-hand side of eqn (1), $\partial T/\partial t$ is also associated, through a temperature-dependent κ/C, with $\nabla^2 T/\rho$. The temperature-dependent ratio κ/C starts to become larger than the value of κ/C measured at room temperature when the temperature increases beyond 55˚C (Table 1). The temperature-dependent κ/C rises to a value 18% (at 90˚C) greater than the ratio at room temperature, which gives rise to the increase in $\partial T/\partial t$. However, the contribution of the temperature-dependent κ/C to the temperature rise is found to be insignificant because the heat conduction (κ/C)$\nabla^2 T$ (in a short time) is overwhelmed by the heat source (H/C).

With the present method, the temperature-dependent thermal parameters (C and κ) are updated according to eqns (3) and (4) on the entire prediction region whenever a new temperature field is predicted. Figure 9 illustrates the temporal variation of the spatial distributions of thermal parameters of liver tissue heated by HIFU for 10 s and then left to cool naturally. The specific heat capacity is initially ($t = 0$ s) a constant value of 3654 J/m^3/K at 25˚C over the entire region, and starts to spatially vary from 3500−3900 J/m^3/K when the tissue is exposed to HIFU (Fig. 9a). Thermal conductivity has an initial constant value of 0.546 W/m/K at 25˚C over the entire region ($t = 0$ s) and starts to spatially vary from 0.52−0.6 W/m/K when the tissue is heated (Fig. 9b). In the present numerical analysis, the maximum temperature rise was less than 90˚C for the range over which measured thermal parameters are currently available. Update of the thermal parameters may be possible by extrapolation unless temperature exceeds the range. Note that the specific heat capacity 3654 J/m^3/K and thermal conductivity 0.546 W/m/K at 25˚C were constant throughout the prediction of the conventional model.

To predict thermal lesions, the contour of temperature at 60˚C was taken as the threshold temperature for thermal necrosis of tissue (Fig. 7). The geometry of the thermal lesion was used as a testing parameter to compare the predictions with the experimental observations. This is because the thermal lesions are visualized in the BSA tissue-mimicking phantom as an opaque region representing its temperature above the threshold (~60˚C) for protein denaturation. In fact, the formation of the thermal lesion depends not only on the temperature but also on the duration, and the two parameters are effectively unified in a quantity called thermal dose. As illustrated in Figures 4−6, the thermal lesion had an ellipsoidal shape and increased in size with exposure time. As expected, the thermal lesions predicted with the method described here (Fig. 9b) were much smaller than those predicted by the conventional method (Fig. 9a). For instance, at an exposure time of 10 s, the present approach predicts 43.5% smaller thermal lesion size than the conventional method. Admitting the present compensation approach is more accurate, treatment planning for HIFU surgery based on the conventional method is likely to lead to insufficient thermal dose settings.

The present study has attempted to compensate for the changes in thermal parameters of tissue with temperature when predicting the temperature distribution of tissue exposed to HIFU. The accuracy of the present prediction is subject to the measured temperature-dependent thermal parameters, and in the present study, these were obtained from an *ex vivo* liver tissue measurement. Such experimental data are not yet readily available for various tissues and the wide ranges of temperatures. It is suggested that future studies will increase our knowledge of the effects of temperature on tissue properties, which will facilitate the compensation of the modification of tissue properties during heating (or cooling) to provide a more accurate prediction of the tissue temperature distribution.

It should be noted that heating causes alterations not only in thermal parameters but also in acoustic parameters. As reported in our previous study, the attenuation coefficient and non-linear parameter (B/A) measured in *ex vivo* liver tissue nearly double as temperatures vary from 50˚C−75˚C (Choi et al. 2011). The compensation of the temperature dependence of the acoustic parameters

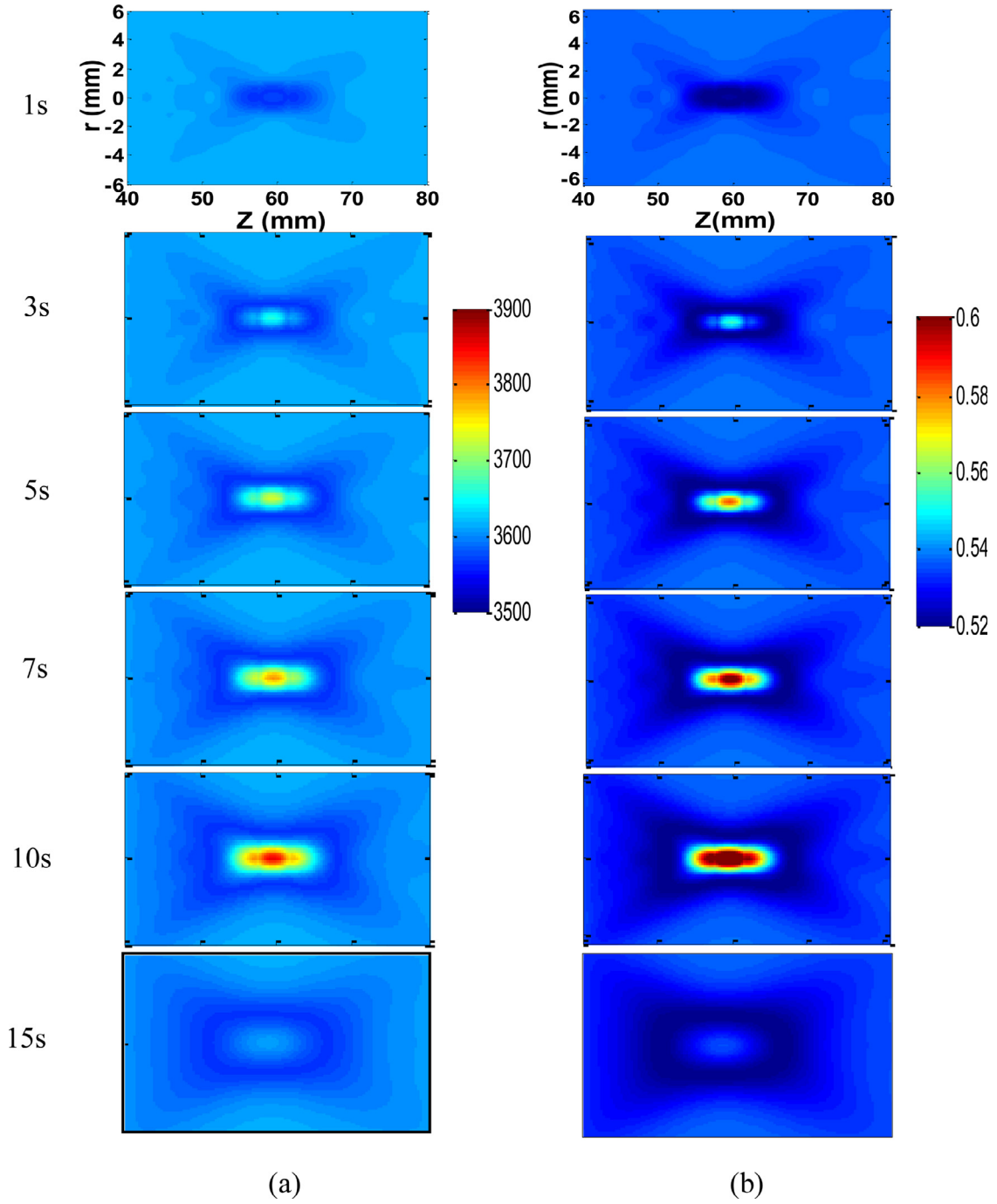

Fig. 9. Temporal variation of the distribution of temperature-dependent thermal parameters in liver exposed to a 1.1-MHz high-intensity ultrasound field with a focal peak pressure of 17.5 MPa for 10 s, followed by 5 s of natural cooling. (a) Specific heat capacity, C ([T*]). (b) Thermal conductivity, k ([T*]).

results in alterations in the acoustic intensity when calculating with the KZK equation, through which the heat source giving rise to the temporal gradient of temperature ($\partial T/\partial t$), the second term on the right-hand side of eqn (1), is modified. The discrepancy between the experimental observation and the present prediction may be in part related to the thermal dependence of the acoustic parameters which are not included in the present numerical analysis. Future work may have to include temperature-dependent acoustic parameters such as the attenuation coefficient, non-linear parameter and speed of sound, as well as the temperature-dependent thermal parameters.

This additional work will yield a more comprehensive numerical model, which effectively compensates for the thermal modification of tissue property, even if it is incomplete yet and still excludes the various thermal effects on tissues of HIFU, such as perfusion, swelling and edema. The various thermal properties and thermal responses of *in vivo* tissues (Johnson et al. 2016; Dillon et al. 2018) obtained using MR thermometry employed in clinical HIFU systems (Gallay et al. 2016) will enable us to verify such a comprehensive model.

CONCLUSIONS

The present study has considered tissue thermal parameters as functions of temperature when predicting the temperature distribution formed in tissue exposed to a surgical HIFU field. Numerical simulation was performed for liver tissue irradiated by the HIFU field. It was found that focal temperature and thermal lesion size were predicted to be significantly lower and smaller, respectively, than those predicted by the conventional method without considering the temperature dependence of the thermal parameters. The results were verified by experimental observation of thermal lesions visualized in a tissue-mimicking phantom exposed to the same HIFU field. The present study claims that the temperature dependence of tissue thermal parameters significantly influences the prediction of temperature rise in tissues exposed to a clinical HIFU field. Accordingly, the temperature dependence of thermal parameters should be considered so as to avoid lower thermal dose settings in HIFU treatment planning.

Acknowledgments—This work was supported by the Korea Evaluation Institute of Industrial Technology (Grant No. 10079270) and the National Research Foundation of Korea (Grant No. 2017R1A2B3007907).

Conflict of interest disclosure—The authors declare no competing interests.

SUPPLEMENTARY MATERIALS

Supplementary material associated with this article can be found in the online version at doi:10.1016/j.ultrasmedbio.2019.10.023.

REFERENCES

Bailey BR, Khokhlova VA, Sapozhnikov OA, Kargl SG, Crum LA. Physical mechanisms of the therapeutic effect of ultrasound. Acoust Phys 2003;49:369–388.

Choi MJ, Guntur SR, Lee JM, Lee KI, Paeng DG, Coleman AJ. Changes in ultrasonic properties of liver tissue in vitro during heating–cooling cycle concomitant with thermal coagulation. Ultrasound Med Biol 2011;37:2000–2012.

Choi MJ, Guntur SR, Lee KI, Paeng DG, Coleman AJ. A tissue mimicking polyacrylamide hydrogel phantom for visualizing thermal lesions generated by high intensity focused ultrasound. Ultrasound Med Biol 2013;29:439–448.

Damianou C, Hynynen K. The effect of various physical parameters on the size and shape of necrosed tissue volume during ultrasound surgery. J Acoust Soc Am 1994;95:1641–1649.

DeSenneville BD, Mougenot C, Quesson B, Dragonu I, Grenier N, Moonen C. MR thermometry for monitoring tumor ablation. Eur Radiol 2007;17:2401–2410.

Dillon CR, Rieke V, Ghanouni P, Payne A. Thermal diffusivity and perfusion constants from *in vivo* MR-guided focused ultrasound treatments: A feasibility study. Int J Hyperthermia 2018;34:352–362.

Dragonu I, de Oliveira PL, Laurent C, Mougenot C, Grenier N, Moonen CT, Quesson B. Non-invasive determination of tissue thermal parameters from high intensity focused ultrasound treatment monitored by volumetric MRI thermometry. NMR Biomed 2009;22:843–851.

Filonenko E, Khokhlova V. Effect of acoustic nonlinearity on heating of biological tissue by high intensity focused ultrasound. Acoust Phys 2001;47:541–549.

Fite BZ, Liu Y, Kruse DE, Caskey CF, Walton JH, Lai CY, Mahakian LM, Larrat B, Dumont E, Ferrara KW. Magnetic resonance thermometry at 7T for real-time monitoring and correction of ultrasound induced mild hyperthermia. Plos One 2012;7 0035509.

Funaki K, Fukunishi H, Sawada K. Clinical outcomes of magnetic resonance-guided focused ultrasound surgery for uterine myomas: 24-month follow-up. Ultrasound Obstet Gynecol 2009;34:584–589.

Gallay MN, Moser D, Rossi F, Pourtehrani P, Magara AE, Kowalski M, Arnold A, Jeanmonod D. Incisionless transcranial MR-guided focused ultrasound in essential tremor: Cerebellothalamic tractotomy. J Ther Ultrasound 2016;13:4–5.

Guntur SR. Tissue mimicking phantoms for visualizing thermal lesions by high intensity focused ultrasound. PhD thesis. Jeju, Korea: Jeju National University; 2013.

Guntur SR, Choi MJ. An improved tissue mimicking polyacrylamide gel for visualization of thermal lesions produced by HIFU. Ultrasound Med Biol 2014;40:2680–2691.

Guntur SR, Choi MJ. Influence of temperature dependent thermal parameters on temperature elevation of tissue exposed to high intensity focused ultrasound: Numerical simulation. Ultrasound Med Biol 2015;40:806–813.

Guntur SR, Lee KI, Paeng DG, Coleman AJ, Choi MJ. Temperature dependent thermal properties of *ex vivo* liver undergoing thermal ablation. Ultrasound Med Biol 2013;39:1771–1784.

Heydari M, Jahed M. Prediction of temperature distribution and volume of lesion during HIFU therapy. In: Proceedings, Sixth International Conference on Information Technology (ITNG 2009), Las Vegas, Nevada, April 27–29, 2009: IEEE; 2009. p. 1468–1473.

Hill CR, ter Haar GR. Review article: High-intensity focused ultrasound—Potential for cancer treatment. Br J Radiol 1995;68:1296–1303.

Johnson SL, Dillon C, Odéen H, Parker D, Christensen D, Payne A. Development and validation of a MRgHIFU noninvasive tissue acoustic property estimation technique. Int J Hyperthermia 2016;32:723–734.

Kobus T, McDannold N. Update on clinical MR guided focused ultrasound applications. Magn Reson Imaging Clin North Am 2015;23:657–667.

Kolios MC, Sherar MD, Hunt JW. Temperature dependent properties and ultrasound thermal therapy. Advances in Heat and Mass Transfer in Biotechnology 1999; HTD-Vol. 363/BED. 44: ASME; 1999. p. 113–118.

Lee KL, Yoon SW. Prediction of the size of a thermal lesion in soft tissue during HIFU treatment. J Kor Phys Soc 2005;47:640–645.

Meaney PM, Clarke RL, ter Haar GR, Rivens IH. A 3-D finite-element model for computation of temperature profiles and regions of thermal damage during focused ultrasound surgery exposures. Ultrasound Med Biol 1998;24:1489–1499.

Park SK, Guntur SR, Lee KI, Paeng DG, Choi MJ. Reusable ultrasonic tissue mimicking hydrogels containing nonionic surface active agent for visualizing thermal lesions. IEEE Trans Biomed Eng 2010;57:194–202.

Pennes HH. Analysis of tissue and arterial blood temperatures in the resting human forearm. J Appl Physiol 1948;1:93–122.

Rieke V, Pauly KB. MR thermometry. J Magn Reson Imaging 2008;27:376–390.

Sapareto SA, Dewey WC. Thermal dose determination in cancer therapy. Int J Radiat Oncol Biol Phys 1984;10:787–800.

ter Haar GR, Sinnett D, Rivens I. High intensity focused ultrasound—A surgical technique for the treatment of discrete liver tumors. Phys Med Biol 1989;34:1743–1750.

Vaezy S, Martin R, Kaczkowski P, Keilman G, Goldman B, Yaziji H, Carter S, Caps M, Crum L. Use of high intensity focused ultrasound to control bleeding. J Vasc Surg 1999;29:533–542.

Zhang J, Hor PH, Fischer J, Partanen A, Karjalainen T, Muthupillai R. A temperature dependent perfusion rate model for simulating temperature evolution in tissue for magnetic resonance imaging guided high intensity focused ultrasound therapy: Initial experience in a pig model. Mag Reson Med 2011;19:3716.

Zhou YF. High intensity focused ultrasound in clinical tumor ablation. World J Clin Oncol 2011;2:8–27.